IVYSPRING INTERNATIONAL PUBLISHER

JOURNAL OF CANCER

2026; 17(11): 1940-1951. doi: 10.7150/jca.138719

Research Paper

[^{177}Lu]Lu-PSMA-617-Mediated Endoradiotherapy of Breast Cancer by Targeting Tumor-Associated Neovasculature

Xiuwei Wu[1,†], Xiaohong Li[2,†], Lili Chen[1], Rou Li[2], Xiao Li[2], Qinqin Yang[2,✉], Maohua Rao[3,✉], Yangchun Chen[4,✉]

1. Department of Oncology, The Second Affiliated Hospital of Anhui Medical University, Hefei 230601, China.
2. Department of Nuclear Medicine, Shanghai Changhai Hospital, Shanghai 200433, China.
3. Department of Nuclear Medicine, Second Affiliated Hospital of Chongqing Medical University, Chongqing 400010, China.
4. Department of Nuclear Medicine, Shanghai Pulmonary Hospital, School of Medicine, Tongji University, Shanghai 200433, China.

†First Author, contributed equally to this work.

✉ Corresponding authors: yangqinqin09@163.com (Qinqin Yang); 304434@hospital.cqmu.edu.cn (Maohua Rao); 2205612@tongji.edu.cn (Yangchun Chen).

© 2026 The Author(s). This is an open access article distributed under the Creative Commons Attribution 4.0 International Licence, subject to the Publisher's Terms of Use at https://ivyspring.com/terms.

Received: 2026.06.02; Accepted: 2026.09.26; Published: 2026.10.25

Abstract

Background: Triple-negative breast cancer (TNBC) is an aggressive subtype lacking effective targeted therapies. Prostate-specific membrane antigen (PSMA) is expressed on the neovasculature of many solid tumors, including breast cancer, making it a potential vascular target for radioligand therapy (RLT). However, whether the therapeutic efficacy of the clinically approved PSMA-targeted radioligand [^{177}Lu]Lu-PSMA-617 in TNBC is strictly dependent on PSMA binding or may involve off-target cross-reactivity (e.g., with fibroblast activation protein, FAP) remains unclear.

Methods: Female BALB/c mice bearing subcutaneous 4T1 TNBC tumors were randomly assigned to four groups (n = 3 each): control (saline), [^{177}Lu]Lu-PSMA-617 alone (18.5 MBq, single intravenous injection), E-urea-K (abbreviated as EK) pre-blocking (excess EK injected 30 min before the radioligand to compete for PSMA binding), and FAPI-04 pre-blocking (FAPI-04 injected 30 min before the radioligand to block FAP). Tumor growth was monitored every two days. SPECT/CT imaging was performed at 1, 4, and 24 h post-injection, and [^{18}F]F-FDG PET/CT was performed on day 7. Tumor tissues were collected for TUNEL apoptosis staining, γ-H2AX immunofluorescence (DNA damage), and PSMA/CD31 co-immunofluorescence.

Results: [^{177}Lu]Lu-PSMA-617 monotherapy significantly suppressed tumor growth, reduced [^{18}F]F-FDG uptake, induced DNA double-strand breaks (γ-H2AX foci) and apoptosis (TUNEL). Moreover, SPECT/CT imaging revealed specific tumor accumulation of [^{177}Lu]Lu-PSMA-617. EK pre-blocking almost completely abolished all these effects, whereas FAPI-04 pre-blocking had no impact. Immunofluorescence revealed PSMA co-localization with CD31 on tumor vascular endothelium, confirming a vascular-targeting mechanism.

Conclusion: The therapeutic efficacy of [^{177}Lu]Lu-PSMA-617 in the 4T1 TNBC model is strictly dependent on specific PSMA binding and is not mediated by FAP cross-reactivity. The radioligand acts primarily by damaging PSMA-positive tumor vasculature, leading to DNA damage, apoptosis, and metabolic inhibition. These findings establish PSMA as a reliable vascular target for RLT in TNBC and support further clinical translation.

Keywords: triple-negative breast cancer, prostate-specific membrane antigen, [^{177}Lu]Lu-PSMA-617, radioligand therapy, tumor angiogenesis

Introduction

Breast cancer remains the most commonly diagnosed malignancy worldwide and the leading cause of cancer-related mortality among women, with an estimated 2.3 million new cases and 764,000 deaths globally in 2023 [1]. Triple-negative breast cancer (TNBC), accounting for 10–20% of all breast cancers, is

among the most aggressive subtypes, with high metastatic capacity and a dismal prognosis [2, 3]. The clinical management of TNBC is particularly challenging due to the absence of estrogen receptor (ER), progesterone receptor (PR), and human epidermal growth factor receptor 2 (HER2) expression. This lack of targetable receptors renders TNBC unresponsive to conventional endocrine therapies and HER2-targeted agents, leaving cytotoxic chemotherapy as the prevailing clinical standard [4, 5]. While patients may respond well initially, over half will relapse within 3 to 5 years after treatment [6, 7]. Despite recent advances with antibody-drug conjugates, CDK4/6 inhibitors, and immune checkpoint inhibitors in specific breast cancer subtypes, resistance and relapse remain major obstacles, and effective therapies for TNBC are still limited [8-10]. Clinically, this aggressive behavior is reflected in the high metastatic potential of TNBC, with approximately 46% of patients eventually developing distant metastases. Pathologically, this propensity for hematogenous dissemination is closely linked to the exceptionally high microvascular density characteristic of this subtype [11-13], which not only facilitates tumor cell intravasation but also underscores the critical role of angiogenesis in TNBC progression.

The process of angiogenesis, which underlies tumor neovascularization, plays a pivotal role in tumor growth, progression, and metastatic dissemination [14, 15]. Consequently, the tumor-associated vasculature has emerged as an attractive therapeutic target [16, 17]. Despite the use of bevacizumab in trials such as AVADO, RIBBON-1, and RIBBON-2, no overall survival benefit has been observed in metastatic breast cancer [18, 19]. These disappointing outcomes underscore the urgent need for alternative therapeutic approaches targeting the tumor vasculature through distinct molecular mechanisms.

Prostate-specific membrane antigen (PSMA) has recently been demonstrated to be widely expressed on the neovasculature endothelium of various solid tumors, including breast cancer, renal cell carcinoma, and glioblastoma, while being virtually absent on normal vascular endothelium [20-23]. In breast cancer, 60-74% of primary tumors and metastatic lesions exhibit PSMA-positive vasculature, which is closely associated with high tumor grade, increased proliferative activity, and poor prognosis [24, 25]. Mechanistic studies have revealed that PSMA promotes endothelial cell invasion and angiogenesis by modulating integrin signaling pathways, and its expression is upregulated under hypoxic conditions and tumor microenvironment stimulation [26, 27].

PSMA ligands developed based on the E-urea-K (abbreviated as EK) structure, such as PSMA-617 and PSMA-I&T, have achieved clinical success in the diagnosis and treatment of prostate cancer [28-31]. [^{177}Lu]Lu-PSMA-617 radioligand therapy significantly prolonged overall survival in patients with metastatic castration-resistant prostate cancer in the phase III VISION trial [30]. Heesch et al. have demonstrated the therapeutic efficacy of [^{177}Lu]Lu-PSMA-I&T in MDA-MB-231 TNBC xenograft models [22]. However, the therapeutic potential of [^{177}Lu]Lu-PSMA-617—the clinically approved specific PSMA ligand—in breast cancer has not been systematically evaluated. More importantly, previous studies have not sufficiently verified whether the therapeutic efficacy is indeed specifically mediated by PSMA or might result from non-tumorous uptake through other tumor-associated molecules, such as fibroblast activation protein (FAP). FAP is highly expressed on cancer-associated fibroblasts in various tumors, and some PSMA ligands may exhibit cross-reactivity [32, 33].

The 4T1 syngeneic breast cancer model exhibits rich neovasculature and can recruit cancer-associated fibroblasts (CAFs) that express high levels of FAP, thereby closely recapitulating the pro-tumorigenic stromal microenvironment of human triple-negative breast cancer [34-36]. Therefore, in this study, tumor-bearing mice of the 4T1 breast cancer model were treated with saline, [^{177}Lu]Lu-PSMA-617 alone, EK injection 30 min prior to [^{177}Lu]Lu-PSMA-617, or FAPI-04 injection 30 min prior to [^{177}Lu]Lu-PSMA-617. By comparing tumor growth inhibition, FDG uptake, and histopathological endpoints among these treatment conditions, we aim to determine whether the therapeutic efficacy of [^{177}Lu]Lu-PSMA-617 is specifically dependent on PSMA binding and to exclude potential non-specific uptake contributions mediated by FAP.

Materials and Methods

Procurement of [^{177}Lu]Lu-PSMA-617 and [^{18}F]F-FDG

A commercially available [^{18}F]F-FDG solution was obtained from Shanghai Atom Kexing Pharmaceutical Co., Ltd. [^{177}Lu]Lu-PSMA-617 injection solution (PLUVICTO®, Advanced Accelerator Applications, Meldola, Italy) was purchased with a radioactive concentration of 1000 MBq/mL at the time of calibration.

Cell culture

The 4T1 cell line (Shanghai Chuan Qiu Biotechnology Co., Ltd, Shanghai, China) was cultured in DMEM (Gibco, Germany) supplemented

with 10% fetal bovine serum and 1% penicillin/streptomycin (Gibco, Germany) at 37 ℃ and 5% CO_2.

Tumor model and study design

All experiments were approved by the Animal Ethics Committee of Shanghai Pulmonary Hospital (K25-004Y), and all methods were carried out in accordance with relevant guidelines and regulations. The reporting in this manuscript adhered to the recommendations in the ARRIVE guidelines.

Female BALB/c mice (Spbif (Beijing) Biotechnology Co., Ltd.) at 6–8 weeks of age were used for syngeneic TNBC tumor model. For each mouse, 1×10^6 4T1 cells were resuspended in a mixture of 100 µL culture medium and 100 µL Matrigel (Corning, NY, USA). Mice were inoculated at the base of the left forelimb. Tumor growth was monitored every two days using caliper measurements. When the tumor volume reached approximately 200 mm^3, the mice were randomly assigned to different treatment groups and the therapy was initiated. The formula for calculating tumor volume is as follows: (length × $width^2$)/2. Tumor volume > 1000 mm^3, mortality, ulceration of tumor tissue, or > 20 % weight loss were defined as humane endpoints.

Animals were randomly distributed into 4 groups: Control (n = 3), [^{177}Lu]Lu-PSMA-617 monotherapy (18.5 MBq) (n = 3), EK pre-blocking (EK, 100 µg per mouse, injected 30 min before the radioligand to compete for PSMA binding) (n = 3), and FAPI-04 pre-blocking (FAPI-04, 100 µg per mouse, injected 30 min before the radioligand to block FAP) (n = 3).

[^{177}Lu]Lu-PSMA-617 therapy

Under anesthesia with 1.5–2.5% isoflurane in medical-grade compressed air at 0.8 L/min, mice received an intravenous injection of [^{177}Lu]Lu-PSMA-617 (18.5 MBq, diluted in 0.9% NaCl to 150 µL) via the lateral tail vein. The administered dose was calculated by subtraction of decay-corrected syringe activity post-injection from preinjection activity.

Small animal SPECT/CT imaging

SPECT/CT imaging (Molecubes γ-Cube/X-Cube) was performed as previously described [37] with the following parameters: 50 kV, 30 µA, 20 min acquisition.

The biodistribution data of [^{177}Lu]Lu-PSMA-617 was used to characterize the organ and tumor time-activity curves. These curves were fitted with mono-exponential curves to enable integration over time, leading to Time Integrated Activity (concentration) Coefficients ([TIAC]). Absorbed doses to the mouse organs and tumor per injected activity (IA) were calculated according to the modified MIRD equation [38]:

$$\frac{D(r_t)}{IA} = \sum_{r_s} [TIAC(r_s)] \times m(r_s) \times S(r_t \leftarrow r_s)$$

with r_t the target organ or tumor, r_s the source organ, $m(r_s)$ the mass of the source organ and $S(r_t \leftarrow r_s)$ the S-value. Both the organ masses and the S-values were taken from the RADAR 25 g mouse phantom [39]. The tumor absorbed doses were calculated by using the sphere S-values from the Olinda dosimetry software [40].

Small animal PET/CT imaging

High-resolution images were acquired using a MadicLab Micro PET/CT system (MadicLab PSA094, Madic Technology, China). Mice were fasted for 8 h and then weighed. Mice were anesthetized with 2% isoflurane at an oxygen flow rate of 1 L/min. After anesthesia, 5.55 MBq of [^{18}F]F-FDG was injected via the tail vein, and the mice were then placed on the scanning bed. For [^{18}F]F-FDG PET/CT, a single scan was performed at 1 h p.i. Image acquisition and reconstruction were performed using MadicLab Acquisition Workplace, which sequentially executes PET acquisition, CT acquisition, PET reconstruction and CT reconstruction.

Image reconstruction was accomplished using a three-dimensional ordered subsets expectation maximization algorithm, followed by maximum a posteriori (MAP), as provided by MadicLab Acquisition Workplace. For each experimental set, three mice were utilized as parallel samples.

H&E staining

After treatment completion, mice were euthanized via overdose anesthesia. Tumor tissues were harvested, fixed in 10% buffered formalin, then dehydrated through graded ethanol, cleared in xylene, and embedded in paraffin. Paraffin-embedded tissues were sectioned at 4 µm, deparaffinized, and subsequently stained with hematoxylin and eosin (H&E). Briefly, sections were stained with Harris hematoxylin for 5–10 min, differentiated in 0.5% acid alcohol for 2–5 sec, blued in dilute ammonia water, then stained with 0.5% eosin for 2–5 min. After dehydration through graded ethanol and clearing in xylene, sections were mounted with neutral resin. H&E-stained sections were imaged using an inverted fluorescence microscope (Olympus BX43, Olympus Corporation, Japan).

TUNEL staining

TUNEL staining was performed according to the

manufacturer's instructions. Briefly, paraffin-embedded tissue sections were deparaffinized in xylene and rehydrated through graded ethanol to distilled water. Sections were then incubated with proteinase K (20 µg/mL) for 15–30 min at 37°C to permeabilize the tissue. After washing with PBS, the TUNEL reaction mixture (containing terminal deoxynucleotidyl transferase and fluorescent-labeled nucleotides) was applied to the sections and incubated for 60 min at 37°C in a humidified chamber. Nuclei were counterstained with DAPI (1 µg/mL) for 5 min. Following thorough washing, slides were mounted with neutral resin. Image acquisition was performed using an inverted fluorescence microscope. TUNEL-positive cells (apoptotic cells) exhibited green fluorescence, while all nuclei were stained blue with DAPI.

Immunohistochemical staining

Immunohistochemical (IHC) staining was performed on formalin-fixed, paraffin-embedded tumor sections using an antibody against γ-H2AX (1:100, 7631S, Cell Signaling Technology, MA, USA). The percentage of γ-H2AX-positive nuclei was quantified to assess DNA double-strand breaks. The average optical density (AOD) of γ-H2AX-positive staining was measured to assess DNA double-strand breaks.

Immunofluorescence staining

Sections were washed with PBS, permeabilized for 5 min with 0.1% Triton X-100/PBS, and blocked for 90 min with 5% goat serum at room temperature. Samples were incubated overnight at 4°C with primary mouse anti-PSMA (1:500, 13163-1-AP, Proteintech, Wuhan, China) or rabbit anti-CD31 (1:2000, ab182981, Abcam, Shanghai, China) antibodies. After washing 3 × with PBS, sections were incubated with goat anti-rabbit Alexa Fluor 488 and goat anti-mouse Alexa Fluor 555 antibodies for 1.5 h at room temperature. Nuclei were counterstained with DAPI for 3 min, and sections were mounted with neutral resin. Image acquisition was performed using an inverted fluorescence microscope.

Quantitative co-localization analysis of PSMA and CD31 immunofluorescence images was performed using the Coloc 2 plugin in Fiji (ImageJ). For each group, three independent tumor sections from three different mice were analyzed. Costes automated thresholding was applied to exclude background signals prior to calculation of Manders' overlap coefficients. The following parameters were reported for each group: Manders' tM1 (the fraction of PSMA-positive pixels overlapping with CD31-positive pixels) and tM2 (the fraction of CD31-positive pixels overlapping with PSMA-positive pixels). Images were acquired under identical exposure and gain settings across all groups.

Statistical analysis

The experimental data were processed using SPSS 23.0 software (SPSS Inc.) and OriginPro 2024b (OriginLab Inc.). Illustrations were created with BioGDP.com [41]. The data are expressed as means ± standard deviation (SD). Normality was assessed using the Shapiro–Wilk test. Student's t test was used for comparisons between two groups of samples, whereas one-way ANOVA was used for comparisons among multiple groups. Significance was determined at the $P < 0.05$ level. All the experiments were performed in triplicate.

Results

[^{177}Lu]Lu-PSMA-617 suppresses 4T1 subcutaneous tumor growth in a PSMA-specific manner

Four groups of 4T1 tumor-bearing BALB/c mice (n = 3 per group) were treated as follows: control (saline), [^{177}Lu]Lu-PSMA-617 alone (18.5 MBq, single intravenous injection), EK pre-blocking (excess EK injected 30 min before the same dose of [^{177}Lu]Lu-PSMA-617), and FAPI-04 pre-blocking (FAPI-04 injected 30 min before the radioligand). The therapeutic effect of [^{177}Lu]Lu-PSMA-617 was analyzed after intravenous administration (**Figure 1A**). Tumor volumes were measured every two days until day 8.

As shown in **Figure 1B, C**, control tumors grew rapidly, reaching a mean volume of 1338.13 ± 86.51 mm^3 on day 8. The [^{177}Lu]Lu-PSMA-617 monotherapy group exhibited significantly suppressed tumor growth, with a mean volume of 840.19 ± 65.69 mm^3 on day 8 (vs. Control, $P < 0.01$). The anti-tumor effect was markedly attenuated by EK pre-blocking (1219.23 ± 52.97 mm^3 on day 8), which was not significantly different from the control group ($P = 0.11$) but significantly higher than the monotherapy group ($P < 0.01$). In contrast, FAPI-04 pre-blocking did not impair the therapeutic effect (929.35 ± 40.74 mm^3 on day 8), remaining significantly lower than the control ($P < 0.01$) and comparable to the monotherapy group ($P = 0.12$). These results indicate that the efficacy of [^{177}Lu]Lu-PSMA-617 depends primarily on specific binding to PSMA, rather than on FAP-mediated non-specific uptake.

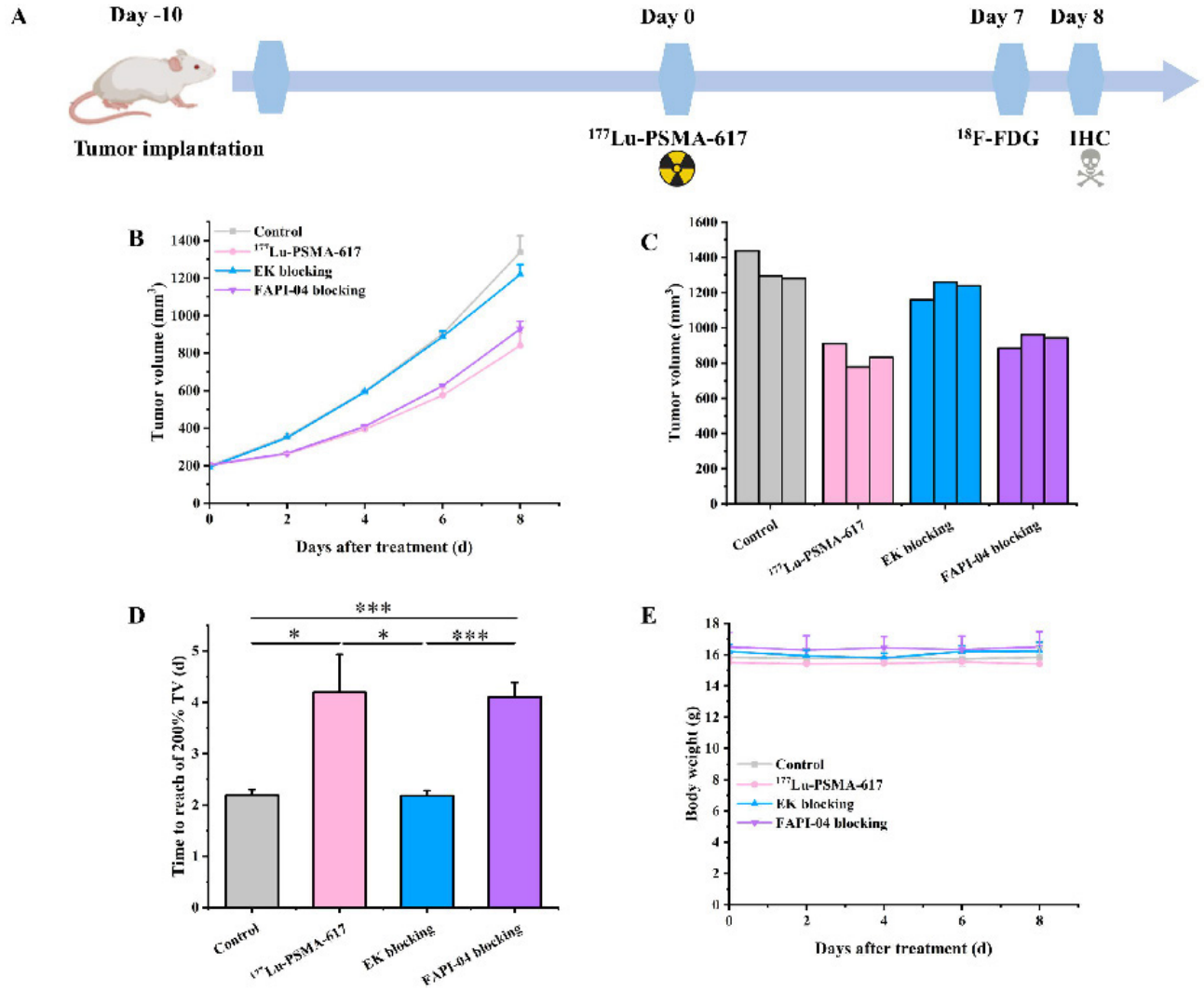

Figure 1. Anti-tumor efficacy of [^{177}Lu]Lu-PSMA-617 in the 4T1 TNBC model. (A) Schematic therapy regime of [^{177}Lu]Lu-PSMA-617. Day 0 marks the start of the treatment. (B) Tumor growth curve in control (gray), [^{177}Lu]Lu-PSMA-617 (pink), EK pre-blocking (blue) and FAPI-04 pre-blocking therapy (violet) animals (n = 3, **P < 0.01). (C) Final tumor volumes on day 8 for each group, presented as mean ± SD (n = 3 per group). (D) Tumor growth analysis comparing the time period (in days) until reaching 200% of the initial tumor volume (TV) in control and therapy-receiving groups. (E) Body weight graphs of 4T1 tumor-bearing mice in different treatment groups.

Moreover, tumor growth was clearly inhibited in the [^{177}Lu]Lu-PSMA-617 monotherapy and FAPI-04 pre-blocking groups, as evidenced by the longer time required to reach 200% of the initial tumor volume compared to the control group (control: 2.19 ± 0.11 days; [^{177}Lu]Lu-PSMA-617 monotherapy: 4.20 ± 0.73 days; FAPI-04 pre-blocking: 4.10 ± 0.29 days; EK pre-blocking: 2.18 ± 0.10 days) (**Figure 1D**). The calculated relative tumor growth inhibition rates on day 8 were 37.21% for the [^{177}Lu]Lu-PSMA-617 monotherapy group and 30.55% for the FAPI-04 pre-blocking group, whereas EK pre-blocking showed only 8.89% inhibition. No significant body weight loss was observed in any of the treatment groups throughout the study period, indicating that the administered dose of [^{177}Lu]Lu-PSMA-617 was well tolerated (**Figure 1E**).

SPECT/CT imaging reveals specific tumor accumulation of [^{177}Lu]Lu-PSMA-617 that is competitively inhibited by EK

SPECT/CT imaging was performed at 1 h, 4 h, and 24 h p.i. (**Figure 2A**). In the [^{177}Lu]Lu-PSMA-617 group, obvious radioactivity accumulation was observed in the tumor as early as 1 h, which already peaked at this time point (1 h %ID/g = 0.34 ± 0.10), followed by a gradual decline at 4 h and 24 h (**Figure 2B**). EK pre-blocking dramatically reduced tumor uptake at all time points (1 h %ID/g = 0.17 ± 0.02), confirming successful competitive blocking of PSMA binding sites (**Figure 2B**). FAPI-04 pre-blocking did not alter tumor uptake (1 h %ID/g = 0.27 ± 0.19) (**Figure 2B**). All groups showed physiological uptake in the kidneys, consistent with the known renal

clearance and PSMA-specific retention of PSMA-targeted ligands (**Figure 2C**). Quantitative analysis of kidney uptake revealed that EK pre-blocking (1 h %ID/g = 0.53 ± 0.30) also reduced renal radioactivity (vs. [^{177}Lu]Lu-PSMA-617, 1 h %ID/g = 1.60 ± 0.73), whereas FAPI-04 pre-blocking had no significant effect (1 h %ID/g = 1.15 ± 0.46), further supporting that the observed tissue accumulation of [^{177}Lu]Lu-PSMA-617 is specifically mediated by PSMA binding (**Figure 2C**). Based on the time-activity curves derived from serial SPECT/CT imaging, the estimated absorbed doses were 3.22 mGy/MBq for the tumor and 10.42 mGy/MBq for the kidney.

Treatment with [^{177}Lu]Lu-PSMA-617 reduces [^{18}F]F-FDG uptake in tumors

On day 7 after [^{177}Lu]Lu-PSMA-617 injection, [^{18}F]F-FDG PET/CT was performed (**Figure 3**). Tumors in the control group exhibited intense FDG uptake, with an SUV_{mean} of 0.58 ± 0.08 (**Figure 3A, B**). [^{177}Lu]Lu-PSMA-617 monotherapy significantly reduced tumor FDG uptake to 0.37 ± 0.03 ($P < 0.01$ vs. control) (**Figure 3A, B**). EK pre-blocking restored FDG uptake to near-control levels (SUV_{mean} = 0.53 ± 0.06, P = 0.55 vs. control), whereas FAPI-04 pre-blocking did not affect the reduction, with the FAPI-04 group showing comparable uptake to the monotherapy group (SUV_{mean} = 0.40 ± 0.02, P = 0.89 vs. monotherapy) (**Figure 3A, B**).

[^{177}Lu]Lu-PSMA-617 induces apoptosis in TNBC tumors

On day 8, tumors were collected for TUNEL apoptosis staining and γ-H2AX immunofluorescence staining (**Figure 4**). The [^{177}Lu]Lu-PSMA-617 group (200.25 ± 16.51) showed a marked increase in the number of apoptotic cells (green fluorescence) in tumor tissues compared to the control group (106.14 ± 16.57) ($P < 0.001$). EK pre-blocking (111.00 ± 20.16) significantly reduced the number of apoptotic cells relative to the [^{177}Lu]Lu-PSMA-617 group (**Figure 4A-D**).

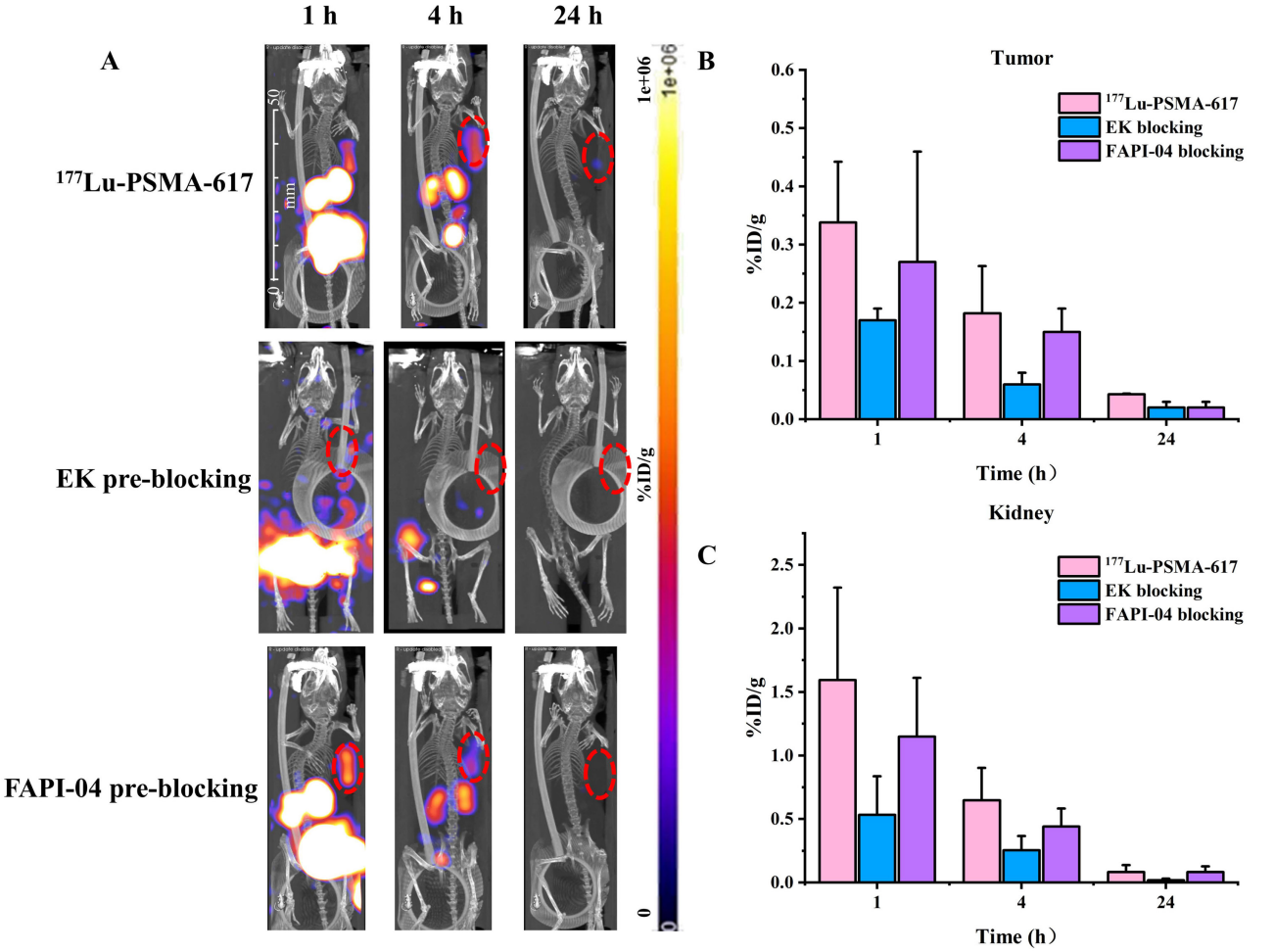

Figure 2. Representative SPECT/CT imaging and quantification of [^{177}Lu]Lu-PSMA-617 tumor uptake in 4T1 tumor-bearing mice. (A) SPECT MIP images of [^{177}Lu]Lu-PSMA-617, EK pre-blocking and FAPI-04 pre-blocking from 1 to 24 h after injection in 4T1 tumor-bearing mice. (B) Corresponding quantification of tumor uptake for each group. (C) Corresponding quantification of kidney uptake for each group.

Similarly, the [^{177}Lu]Lu-PSMA-617 group (0.268 ± 0.024) exhibited abundant γ-H2AX foci (a marker of DNA double-strand breaks) in tumor cell nuclei compared to the control group (0.060 ± 0.007) ($P < 0.001$). EK pre-blocking (0.121 ± 0.013) markedly reduced the number of γ-H2AX signal intensity (**Figure 4E-H**). These results demonstrate that [^{177}Lu]Lu-PSMA-617 induces DNA damage and subsequent apoptosis in a strictly PSMA-dependent manner.

[^{177}Lu]Lu-PSMA-617 binds to tumor-associated vasculature in TNBC

H&E staining revealed notable histopathological changes in tumor tissues (**Figure 5A-C**). Compared to the control group, tumors from the treatment groups exhibited more necrotic tissue (light pink) and fewer viable areas. Immunofluorescence co-staining for PSMA and CD31 was performed on tumor sections collected on day 8 (**Figure 5D-F**). In the control and monotherapy groups, PSMA (red) clearly co-localized with CD31 (green) on tumor vascular endothelium (yellow overlay), confirming that PSMA is predominantly expressed on neovasculature (**Figure 5D-E**). EK pre-blocking did not alter PSMA/CD31 expression levels; however, the reduced SPECT uptake confirmed competitive occupancy of the binding sites (**Figure 5F**).

To validate the vascular localization of PSMA, quantitative co-localization analysis of PSMA and CD31 immunofluorescence was performed on tumor sections from the control, [^{177}Lu]Lu-PSMA-617 monotherapy, and EK pre-blocking groups. In control tumors, PSMA and CD31 showed substantial overlap, with Manders' coefficients of tM1 = 0.59 ± 0.07 and tM2 = 0.59 ± 0.06, confirming that PSMA is predominantly expressed on CD31-positive vascular endothelium (**Figure 5G, J**). Following [^{177}Lu]Lu-PSMA-617 treatment, Manders' coefficients were tM1 = 0.84 ± 0.10 and tM2 = 0.47 ± 0.08 (**Figure 5H, J**). The high tM1 indicates sustained PSMA localization to CD31-positive vascular regions after radioligand treatment, while the decreased CD31 mean intensity (19.18 ± 1.18 vs. 35.94 ± 3.75 in control) and reduced PSMA mean intensity (24.13 ± 2.17 vs. 47.47 ± 4.38 in control) reflects radiation-induced vascular disruption, consistent with the observed therapeutic efficacy (**Figure 5K**). In contrast, EK pre-blocking preserved vascular integrity to near-control levels (tM2 = 0.58 ± 0.08, CD31 mean intensity = 36.31 ± 4.06 vs. 35.94 ± 3.75 in controls), indicating that this integrity is maintained in the absence of effective PSMA-targeted therapy (**Figure 5I-K**). However, PSMA mean intensity in the EK pre-blocking group (36.32 ± 2.95) remained lower than that in controls (47.47 ± 4.38), despite preserved CD31 signal. This partial reduction is most likely due to epitope masking by EK occupying the PSMA binding site, rather than true downregulation of PSMA expression, as supported by the nearly complete blockade of tumor uptake on SPECT/CT in this group (Figure 2). Collectively, these data reinforce that PSMA-specific binding is the essential prerequisite for anti-tumor efficacy.

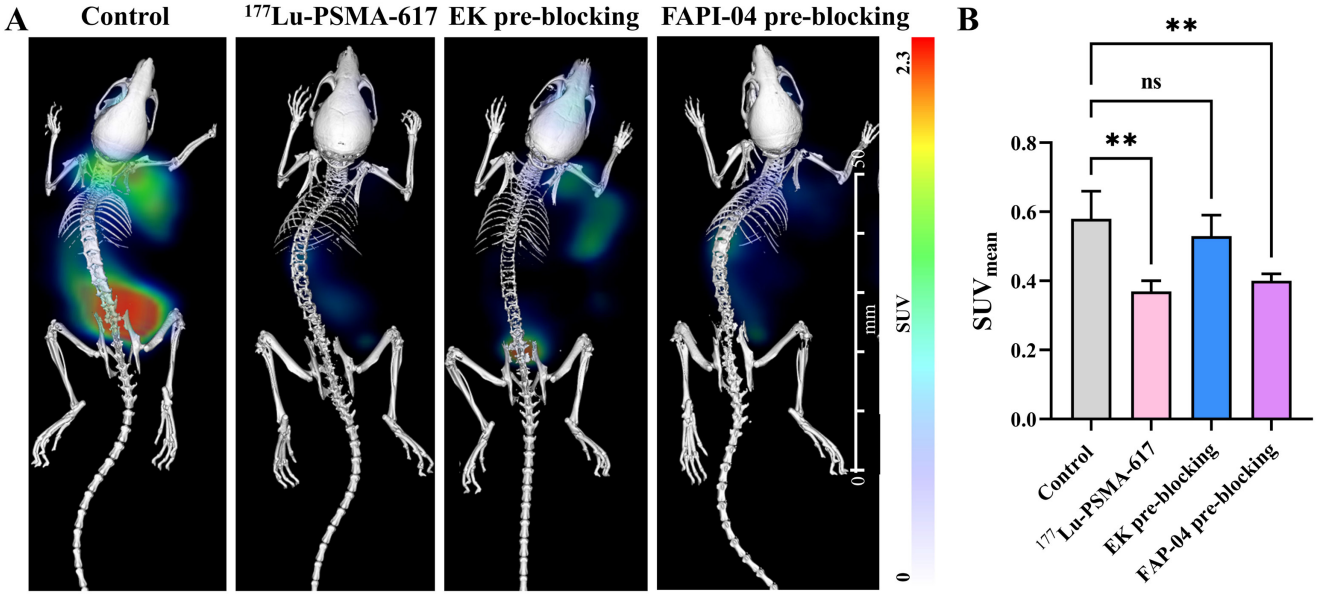

Figure 3. [^{18}F]F-FDG PET/CT imaging and quantification of tumor glucose metabolism after [^{177}Lu]Lu-PSMA-617 therapy. (A) Representative PET/CT images of [^{18}F]F-FDG distribution 1 h post injection in control, [^{177}Lu]Lu-PSMA-617, EK pre-blocking, and FAPI-04 pre-blocking group 7 d after therapy. (B) PET quantification data of [^{18}F]F-FDG uptake in different groups of 4T1 tumor-bearing mice. Data are presented as mean ± SD (n = 3 per group). **P < 0.01; ns, not significant.

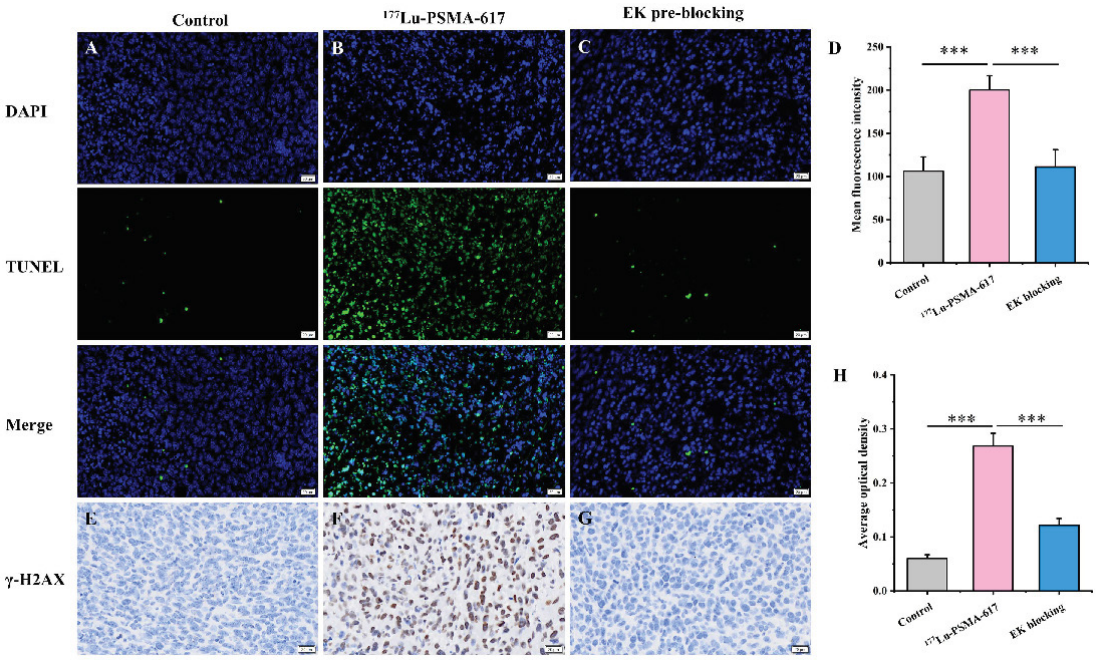

Figure 4. [177Lu]Lu-PSMA-617 induces apoptosis and DNA damage in a PSMA-dependent manner. Microscopic evaluation of TUNEL (green) expression in tumor tissue from control (A), [177Lu]Lu-PSMA-617 (B), and EK pre-blocking (C) animals. (D) Representative histograms showing the mean fluorescence intensity of TUNEL-positive signals. Nuclei were counterstained with DAPI (blue). Scale bar: 20 μm. Immunohistochemical staining of γ-H2AX in tumor tissues from control (E), [177Lu]Lu-PSMA-617 (F), and EK pre-blocking (G) animals. Scale bar: 20 μm. (H) γ-H2AX expression was quantified by calculating the average optical density (AOD), defined as the integrated optical density divided by the area of the region of interest (AOD = Integrated optical density / Area).

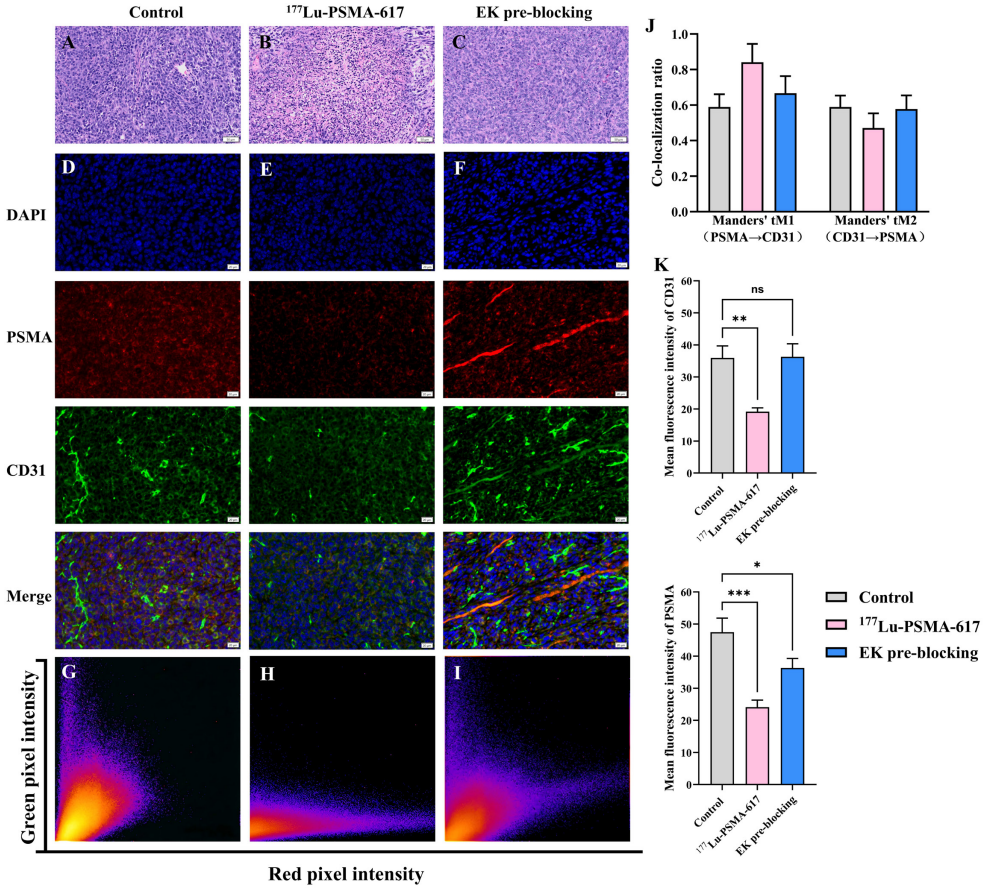

Figure 5. Histological and immunofluorescence analysis of tumor tissues. H&E-stained tumor sections from mice in different groups (A–C). Scale bar: 50 μm. (D-F) Staining of tumor tissues to show DAPI staining (blue), PSMA (red) and CD31 (green). The "Merge" showing co-localization of PSMA-CD31 in the tumor tissues showing PSMA expression in 4T1 neovasculature. Images captured at 20 × magnification; measurement bars represent 20 μm. (G-I) Representative co-localization images showing PSMA/CD31 co-localization in control, monotherapy, and EK pre-blocking groups, respectively. (J) Quantitative analysis of Manders' overlap coefficients (tM1 and tM2) for each group. (K) Quantitative analysis of mean fluorescence intensities of PSMA (red) and CD31 (green) for each group.

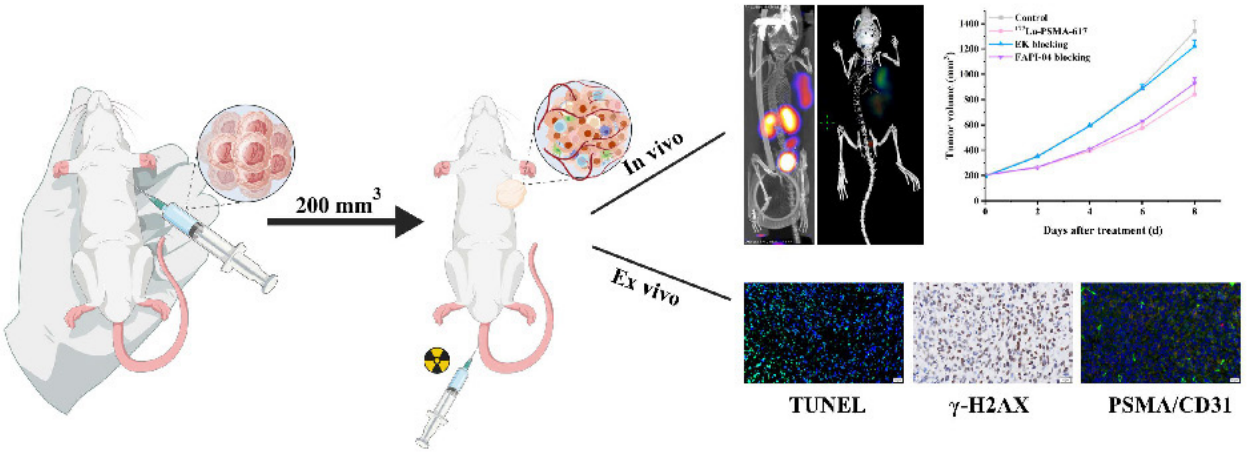

Figure 6. Graphical abstract of the therapeutic efficacy and vascular targeting mechanism of [^{177}Lu]Lu-PSMA-617 in a 4T1 model.

Discussion

This study is the first to employ a dual-blockade design incorporating both PSMA-specific blockade and FAP blockade, thereby providing the possibility to validate the PSMA-specific targeted therapeutic effect of [^{177}Lu]Lu-PSMA-617 in the 4T1 breast cancer model, and offering new experimental evidence for establishing PSMA as a reliable molecular target for vascular-directed therapy of breast cancer. To achieve this, we employed a dual-blockade design using EK (PSMA-specific competitor) and FAPI-04 (FAP blocker) to rigorously investigate whether the therapeutic efficacy of the clinically approved radioligand [^{177}Lu]Lu-PSMA-617 in a 4T1 breast cancer model depends on specific PSMA binding. Our results demonstrate that a single 18.5 MBq dose of [^{177}Lu]Lu-PSMA-617 significantly suppressed tumor growth, reduced glucose metabolism, induced DNA double-strand breaks and apoptosis, and specifically accumulated in tumor vasculature. Importantly, EK pre-blocking almost completely abolished all these therapeutic and imaging outcomes, whereas FAPI-04 pre-blocking had no effect. These findings provide strong evidence that the anti-tumor activity of [^{177}Lu]Lu-PSMA-617 in 4T1 tumors is strictly dependent on PSMA binding and not mediated by cross-reactivity with FAP or other non-specific mechanisms.

Triple-negative breast cancer (TNBC) is characterized by aggressive behavior, high metastatic potential, and a lack of effective targeted therapies [42, 43]. Anti-angiogenic strategies targeting VEGF have failed to improve overall survival in breast cancer, highlighting the need for alternative vascular-directed approaches [18, 19]. PSMA is highly expressed on the neovasculature of many solid tumors, including breast cancer, but is virtually absent on normal endothelium [21, 44]. Our immunofluorescence co-localization of PSMA with CD31 confirms that PSMA is expressed on tumor vascular endothelial cells in the 4T1 model, and SPECT/CT imaging shows that [^{177}Lu]Lu-PSMA-617 predominantly accumulates at these vascular sites. Therefore, the therapeutic effect of PSMA-targeted radioligand therapy (RLT) in this setting is largely mediated by damage to tumor-associated endothelium, leading to secondary tumor ischemia, necrosis, and apoptosis.

The tumor absorbed dose estimated in this study (3.22 mGy/MBq) is comparable to the pooled mean tumor dose reported for [^{177}Lu]Lu-PSMA-617 in soft-tissue prostate cancer lesions (4.19 Gy/GBq) in a recent systematic review and meta-analysis [45]. Although the SPECT-measured tumor uptake was modest, the β-particle cross-fire effect, with a maximum tissue range of approximately 2 mm, allows radiation damage to extend from the PSMA-positive vascular endothelium to adjacent tumor cells. This mechanism is consistent with the preserved PSMA/CD31 co-localization and the radiation-induced vascular disruption observed after monotherapy. The near-complete abrogation of efficacy by EK pre-blocking further confirms that the therapeutic effect is PSMA-specific and not driven by secondary systemic effects.

The partial reduction in PSMA immunofluorescence observed in the EK pre-blocking group is most likely attributable to epitope masking rather than to a true decrease in PSMA protein expression. Since EK is a PSMA-binding ligand, its occupancy of the PSMA active site can sterically hinder binding of the anti-PSMA antibody used for immunofluorescence detection, thereby reducing the apparent signal even when PSMA protein levels remain unchanged. This mechanism also explains the discordance between preserved CD31-positive vascular structures and the mildly reduced PSMA

signal in this group. The SPECT/CT findings support this interpretation, as EK pre-blocking almost completely abolished tumor uptake, confirming effective occupancy of PSMA binding sites *in vivo*. Taken together, the changes in PSMA signal intensity shown in Figure 5K are likely to reflect a combination of radiation-induced vascular loss in the monotherapy group and ligand-mediated epitope masking in the EK group, rather than a true downregulation of PSMA protein expression.

A point requiring careful consideration is the species selectivity of [^{177}Lu]Lu-PSMA-617. It is well established that this radioligand exhibits substantially lower binding affinity for murine PSMA than for its human counterpart, with reported KD values of 2.33 nM for human PSMA and 138 nM for murine PSMA [46, 47]. Although this species difference might initially raise questions regarding the translational relevance of the syngeneic 4T1 model, several lines of evidence from the present study support the validity of our observations. PSMA expression in this model is predominantly restricted to the tumor-associated neovasculature rather than to the tumor cells themselves. The localized vascular accumulation of the radioligand, as visualized by SPECT/CT imaging (Figure 2), enables a sufficient radiation dose to be delivered to the endothelial compartment even in the setting of reduced affinity. The cross-fire effect of β-particles, with a maximum tissue range of approximately 2 mm, permits radiation damage to extend beyond the immediate binding sites, affecting adjacent endothelial and tumor cells. Most critically, the near-complete abrogation of both tumor uptake and therapeutic response by EK pre-administration (Figures 1–2) provides direct functional evidence that the observed effects are specifically PSMA-mediated, irrespective of the absolute affinity for the murine orthologue. Collectively, these findings indicate that while the 4T1 model does not recapitulate the high-affinity human PSMA interaction, it remains a valid system for investigating the vascular-targeting mechanism of PSMA-directed radioligand therapy, particularly when pharmacological blockade is used as a specificity control.

Consistent with the reported pattern, TUNEL-positive apoptotic cells were enriched at the tumor periphery; in contrast, γ-H2AX foci were distributed more evenly throughout the tumor. The periphery is generally better vascularized and oxygenated, which may render it more susceptible to radiation-induced DNA damage and apoptosis. Central necrosis may result from secondary ischemic injury following vascular disruption. Moreover, the significant decrease in [^{18}F]F-FDG uptake at day 7 suggests that [^{177}Lu]Lu-PSMA-617 rapidly impairs tumor viability.

Our work offers several advances. We used the clinically approved PSMA-617, which has higher translational relevance. Furthermore, we employed an immunocompetent 4T1 syngeneic model that preserves tumor-microenvironment interactions, unlike the xenograft model. In addition, we included both PSMA-specific (EK) and FAP-specific (FAPI-04) blockade groups to definitively exclude the possibility of off-target FAP binding. Although some reports have suggested possible cross-reactivity of PSMA ligands with FAP [32], our data clearly rule out this possibility in the 4T1 model.

Several limitations of this study should be acknowledged. The sample size of three animals per group, while adequate for a proof-of-concept mechanistic evaluation, limits the statistical power for precisely estimating therapeutic effect sizes. Nevertheless, the consistently observed trends across multiple orthogonal endpoints, including tumor volumetry, SPECT/CT imaging, PET/CT metabolic assessment, and histopathological analyses, support the reliability of the findings. The substantially lower affinity of [^{177}Lu]Lu-PSMA-617 for murine PSMA compared to human PSMA represents a caveat in interpreting the translational potential of our observations; however, the near-complete abrogation of therapeutic efficacy by EK pre-administration confirms that the effects are specifically PSMA-mediated. Although 4T1 cells themselves express very low levels of PSMA and the therapeutic effect is attributed primarily to vascular targeting, a minor direct effect on PSMA-positive tumor cells cannot be completely excluded [23]. In addition, long-term radiotoxicity and repeated dosing schedules were not evaluated in this acute single-administration study. Future studies with larger, adequately powered cohorts, consisting of 5–6 mice per group, will be necessary to confirm the therapeutic efficacy, evaluate long-term safety and fractionated dosing regimens, and explore combination strategies, for example with immunotherapy, in additional TNBC models.

Conclusions

This study, for the first time, employs a dual-blockade design with EK (PSMA-specific competitor) and FAPI-04 (FAP blocker) to demonstrate that the therapeutic efficacy of [^{177}Lu]Lu-PSMA-617 in the 4T1 subcutaneous triple-negative breast cancer model is strictly dependent on specific PSMA binding, rather than on FAP-mediated non-specific uptake. [^{177}Lu]Lu-PSMA-617 predominantly localizes to tumor-associated vascular endothelium, where it induces DNA damage and apoptosis, leading to

inhibition of tumor growth and glucose metabolism. These findings provide critical experimental evidence establishing PSMA as a reliable molecular target for vascular-directed radioligand therapy in TNBC, and they exclude potential interference from FAP cross-reactivity, thereby supporting clinical translation.

Abbreviations

TNBC: triple-negative breast cancer; PSMA: prostate-specific membrane antigen; RLT: radioligand therapy; FAP: fibroblast activation protein; ER: estrogen receptor; PR: progesterone receptor; HER2: human epidermal growth factor receptor 2; VEGF: vascular endothelial growth factor; EK: E-urea-K; CAF: cancer-associated fibroblasts.

Acknowledgments

This research was funded by the National Natural Science Foundation Youth Project (82402423), Tongji University Medicine-X Interdisciplinary Research Initiative (2025-0554-YB-11), and Chongqing Municipal Science and Health Joint Medical Research General Program: Construction of a Precision Assessment System for Renal Fibrosis Using Combined Multimodal Imaging (2026MSXM156).

Authorship contribution statement

Xiuwei Wu: Data curation, Investigation, Writing – original draft. **Xiaohong Li**: Data curation, Investigation, Visualization. **Lili Chen**: Data curation, Investigation. **Rou Li**: Data curation, Investigation, Funding acquisition. **Xiao Li**: Data curation, Investigation. **Qinqin Yang**: Writing – original draft, Data curation, Investigation. **Maohua Rao**: Resources, Supervision, Writing – review & editing, Funding acquisition. **Yangchun Chen**: Conceptualization, Resources, Supervision, Writing – review & editing, Funding acquisition.

Data availability

Data will be made available on request.

Competing Interests

The authors have declared that no competing interest exists.

References

1. GBD 2023 Breast Cancer Collaborators. Global, regional, and national burden of breast cancer among females, 1990-2023, with forecasts to 2050: a systematic analysis for the Global Burden of Disease Study 2023. Lancet Oncol. 2026; 27(3): 302-326.
2. Stern S, Liang D, Li L, Kurian R, Lynch C, Sakamuru S, et al. Targeting CAR and Nrf2 improves cyclophosphamide bioactivation while reducing doxorubicin-induced cardiotoxicity in triple-negative breast cancer treatment. JCI insight. 2022; 7: e153868.
3. Chen YY, Ge JY, Zhu SY, Shao ZM, Yu KD. Copy number amplification of ENSA promotes the progression of triple-negative breast cancer via cholesterol biosynthesis. Nature communications. 2022; 13: 791.
4. Luo M, Fu A, Wu R, Wei N, Song K, Lim S, et al. High Expression of G6PD Increases Doxorubicin Resistance in Triple Negative Breast Cancer Cells by Maintaining GSH Level. International journal of biological sciences. 2022; 18: 1120-33.
5. Naik A, Decock J. Targeting of lactate dehydrogenase C dysregulates the cell cycle and sensitizes breast cancer cells to DNA damage response targeted therapy. Molecular oncology. 2022; 16: 885-903.
6. Yu B, Luo F, Sun B, Liu W, Shi Q, Cheng SY, et al. KAT6A Acetylation of SMAD3 Regulates Myeloid-Derived Suppressor Cell Recruitment, Metastasis, and Immunotherapy in Triple-Negative Breast Cancer. Advanced science (Weinheim, Baden-Wurttemberg, Germany). 2021; 8: e2100014.
7. Lin LF, Li YT, Han H, Lin SG. MicroRNA-205-5p targets the HOXD9-Snail1 axis to inhibit triple negative breast cancer cell proliferation and chemoresistance. Aging. 2021; 13: 3945-56.
8. Zhao H, Zhou X, Wang G, Yu Y, Li Y, Chen Z, et al. Integrating Bulk and Single-cell RNA-seq to Construct a Macrophage-related Prognostic Model for Prognostic Stratification in Triple-negative Breast Cancer. J Cancer. 2024;15: 6002-6015.
9. Wang GX, Cao JM, Lu CL, Wang YL, Chen ZY, Yang CQ, et al. Integrative multi-omics and radiomics reveal a TMSB10-driven cell state for non-invasive assessment and precision stratification in breast cancer. Front Immunol. 2026;17: 1794329.
10. Wang G, Cao J, Lu C, Cao Y, Wang S, Chen Z, et al. Multiomics profiling identifies the poor prognostic role of a tumor cluster with GNA15 overexpression in triple-negative breast cancer. Front Immunol. 2025;16: 1659183.
11. Aspros KGM, Carter JM, Hoskin TL, Suman VJ, Subramaniam M, Emch MJ, et al. Estrogen receptor beta repurposes EZH2 to suppress oncogenic NFκB/p65 signaling in triple negative breast cancer. NPJ breast cancer. 2022; 8: 20.
12. Goyal AV, Shukla S, Acharya S, Vagha S, Jajoo S. Correlation of microvessel density with histopathological parameters of carcinoma breast. The Indian journal of medical research. 2023; 158: 417-22.
13. El-Houjeiri L, Biondini M, Paquette M, Kuasne H, Pacis A, Park M, et al. Folliculin impairs breast tumor growth by repressing TFE3-dependent induction of the Warburg effect and angiogenesis. The Journal of clinical investigation. 2021; 131: e144871.
14. Li S, Nguyen TT, Ung TT, Sah DK, Park SY, Lakshmanan VK, et al. Piperine Attenuates Lithocholic Acid-Stimulated Interleukin-8 by Suppressing Src/EGFR and Reactive Oxygen Species in Human Colorectal Cancer Cells. Antioxidants (Basel, Switzerland). 2022; 11: 530.
15. Şen Ö, Marino A, Pucci C, Ciofani G. Modulation of anti-angiogenic activity using ultrasound-activated nutlin-loaded piezoelectric nanovectors. Materials today Bio. 2022; 13: 100196.
16. Yang F, Lee G, Fan Y. Navigating tumor angiogenesis: therapeutic perspectives and myeloid cell regulation mechanism. Angiogenesis. 2024; 27: 333-49.
17. Pan X, Li X, Dong L, Liu T, Zhang M, Zhang L, et al. Tumour vasculature at single-cell resolution. Nature. 2024; 632: 429-36.
18. Yamamoto Y, Yamashiro H, Schneeweiss A, Müller V, Gluz O, Klare P, et al. Factors affecting prognosis in patients treated with bevacizumab plus paclitaxel as first-line chemotherapy for HER2-negative metastatic breast cancer: an international pooled analysis of individual patient data from four prospective observational studies. Breast cancer (Tokyo, Japan). 2023; 30: 88-100.
19. Alvarez RH, Guarneri V, Icli F, Johnston S, Khayat D, Loibl S, et al. Bevacizumab treatment for advanced breast cancer. The oncologist. 2011; 16: 1684-97.
20. Li Y, Zhang K, Yang F, Jiao D, Li M, Zhao X, et al. Prognostic Value of Vascular-Expressed PSMA and CD248 in Urothelial Carcinoma of the Bladder. Frontiers in oncology. 2021; 11: 771036.
21. Chen Y, Minn I, Rowe SP, Lisok A, Chatterjee S, Brummet M, et al. A Series of PSMA-Targeted Near-Infrared Fluorescent Imaging Agents. Biomolecules. 2022; 12: 405.
22. Heesch A, Florea A, Maurer J, Habib P, Werth LS, Hansen T, et al. The prostate-specific membrane antigen holds potential as a vascular target for endogenous radiotherapy with [(177)Lu]Lu-PSMA-I&T for triple-negative breast cancer. Breast cancer research : BCR. 2024; 26: 30.
23. Shirke AA, Wang J, Ramamurthy G, Mahanty A, Walker E, Zhang L, et al. Prostate Specific Membrane Antigen Expression in a Syngeneic Breast Cancer Mouse Model. Molecular imaging and biology. 2024; 26: 714-28.
24. Van de Wiele C, Sathekge M, de Spiegeleer B, De Jonghe PJ, Debruyne PR, Borms M, et al. PSMA expression on neovasculature of solid tumors. Histology and histopathology. 2020; 35: 919-27.
25. Puik JR, Le C, Kazemier G, Oprea-Lager DE, Swijnenburg RJ, Giovannetti E, et al. Prostate-specific membrane antigen as target for vasculature-directed therapeutic strategies in solid tumors. Critical reviews in oncology/hematology. 2025; 205: 104556.
26. Heesch A, Ortmanns L, Maurer J, Stickeler E, Sahnoun SEM, Mottaghy FM, et al. The Potential of PSMA as a Vascular Target in TNBC. Cells. 2023; 12: 551.
27. Watanabe R, Maekawa M, Kiyoi T, Kurata M, Miura N, Kikugawa T, et al. PSMA-positive membranes secreted from prostate cancer cells have potency to transform vascular endothelial cells into an angiogenic state. The Prostate. 2021; 81: 1390-401.

28. Wang L, Ren S, Lou J, Xue S, Zhou P, Zheng X, et al. E-Urea-K-Based PSMA Imaging Served as an Alternative in Assessing Tumor Neovascularization via Targeting CD31. Molecular pharmaceutics. 2025; 22: 2029-39.
29. Burkett BJ. Radioligand Therapy for Metastatic Prostate Cancer. Radiology Imaging cancer. 2021; 3: e219026.
30. Sartor O, de Bono J, Chi KN, Fizazi K, Herrmann K, Rahbar K, et al. Lutetium-177-PSMA-617 for Metastatic Castration-Resistant Prostate Cancer. The New England journal of medicine. 2021; 385: 1091-103.
31. Hartrampf PE, Seitz AK, Weinzierl FX, Serfling SE, Schirbel A, Rowe SP, et al. Baseline clinical characteristics predict overall survival in patients undergoing radioligand therapy with [(177)Lu]Lu-PSMA I&T during long-term follow-up. European journal of nuclear medicine and molecular imaging. 2022; 49: 4262-70.
32. Verena A, Zhang Z, Kuo HT, Merkens H, Zeisler J, Wilson R, et al. Synthesis and Preclinical Evaluation of Three Novel 68Ga-Labeled Bispecific PSMA/FAP-Targeting Tracers for Prostate Cancer Imaging. Molecules. 2023; 28: 1088.
33. Zang J, Wen X, Lin R, Zeng X, Wang C, Shi M, et al. Synthesis, preclinical evaluation and radiation dosimetry of a dual targeting PET tracer [(68)Ga]Ga-FAPI-RGD. Theranostics. 2022; 12: 7180-90.
34. Malekian S, Rahmati M, Sari S, Kazemimanesh M, Kheirbakhsh R, Muhammadnejad A, et al. Expression of Diverse Angiogenesis Factor in Different Stages of the 4T1 Tumor as a Mouse Model of Triple-Negative Breast Cancer. Advanced pharmaceutical bulletin. 2020; 10: 323-8.
35. Venning FA, Zornhagen KW, Wullkopf L, Sjölund J, Rodriguez-Cupello C, Kjellman P, et al. Deciphering the temporal heterogeneity of cancer-associated fibroblast subpopulations in breast cancer. Journal of experimental & clinical cancer research : CR. 2021; 40: 175.
36. Chen M, Xiao L, Jia H, Wang S, Jiang X, Lei X, et al. Stereotactic ablative radiotherapy and FAPα-based cancer vaccine suppresses metastatic tumor growth in 4T1 mouse breast cancer. Radiotherapy and oncology : journal of the European Society for Therapeutic Radiology and Oncology. 2023; 189: 109946.
37. Zheng X, Xue S, Zhao Z, Jin S, He S, Jia L, et al. The development of (177)Lu-DOTA-CC-PSMA following a unified "Click Chemistry" protocol of synthesizing metal nuclide-conjugated radiopharmaceuticals. EJNMMI radiopharmacy and chemistry. 2024; 9: 56.
38. van der Heide CD, Ntihabose CM, Konijnenberg M, Ma H, Stuurman D, de Ridder C, et al. Head-to-head comparison of [177Lu]Lu-FAP-2286 and [161Tb]Tb-FAP-2286 efficacy in a PDAC mouse model. EJNMMI Res. 2026; 16: 29.
39. Keenan MA, Stabin MG, Segars WP, Fernald MJ. RADAR realistic animal model series for dose assessment. J Nucl Med. 2010; 51: 471-476.
40. Stabin MG, Konijnenberg MW. Re-evaluation of absorbed fractions for photons and electrons in spheres of various sizes. J Nucl Med. 2000; 41: 149-160.
41. Jiang S, Li H, Zhang L, Mu W, Zhang Y, Chen T, et al. Generic Diagramming Platform (GDP): a comprehensive database of high-quality biomedical graphics. Nucleic Acids Research. 2025; 53: D1670-D6.
42. Li Y, Wu J, Qiu X, Dong S, He J, Liu J, et al. Bacterial outer membrane vesicles-based therapeutic platform eradicates triple-negative breast tumor by combinational photodynamic/chemo-/immunotherapy. Bioactive materials. 2023; 20: 548-60.
43. Kamin H, Nolte L, Bleilevens A, Stickeler E, Heinemann D, Maurer J, et al. Imaging and quantification of the tumor microenvironment of triple negative breast cancer using TPEF and scanning laser optical tomography. Biomedical optics express. 2023; 14: 4579-93.
44. Hu K, Li L, Huang Y, Ye S, Zhong J, Yan Q, et al. Radiosynthesis and Preclinical Evaluation of Bispecific PSMA/FAP Heterodimers for Tumor Imaging. Pharmaceuticals (Basel, Switzerland). 2022; 15: 383.
45. Ells Z, Grogan TR, Czernin J, Dahlbom M, Calais J. Dosimetry of [177Lu]Lu-PSMA-Targeted Radiopharmaceutical Therapies in Patients with Prostate Cancer: A Comparative Systematic Review and Metaanalysis. J Nucl Med. 2024; 65: 1264-1271.
46. Wen X, Xu P, Zeng X, Liu J, Du C, Zeng X, et al. Development of [177Lu]Lu-LNC1003 for radioligand therapy of prostate cancer with a moderate level of PSMA expression. Eur J Nucl Med Mol Imaging. 2023;50: 2846-2860.
47. Richard M, Louis B, Taddio MF, Jeanjean P, Diaz Garcia-Prada C, Swaidan A, et al. Development of Radioligand Therapy-Responsive Syngeneic Prostate Models through Murine Prostate-Specific Membrane Antigen Point Mutation. ACS Pharmacol Transl Sci. 2026;9: 1767-1782.